Mechanistic Insight into the Photo-Oxidation of Perfluorocarboxylic Acid over Boron Nitride

Yu Chen,[#] Manav Bhati,[#] Benjamin W. Walls, Bo Wang, Michael S. Wong, and Thomas P. Senftle*

ACCESS | Metrics & More | Article Recommendations | Supporting Information

ABSTRACT: Hexagonal boron nitride (hBN) can photocatalytically oxidize and degrade perfluorocarboxylic acids (PFCA), a common member of the per/polyfluoroalkyl substance (PFAS) family of water contaminants. However, the reaction mechanism governing PFCA activation on hBN is not yet understood. Here, we apply electronic grand canonical density functional theory (GC-DFT) to assess the thermodynamic and kinetic favorability of PFCA photo-oxidative activation on hBN: $C_nF_{2n+1}COO^- + h^+ \rightarrow C_nF_{2n+1}^{\cdot} + CO_2$. The oxidation of all PFCA chains is exothermic under illumination with a moderate barrier. However, the longer-chain PFCAs are degraded more effectively because they adsorb on the surface more strongly as a result of increased van der Waals interactions with the hBN surface. The ability of hBN to act as a photocatalyst is unexpected because of its wide band gap. Therefore, we apply both theoretical and experimental analyses to examine possible defects on hBN that could account for its activity. We find that a nitrogen-boron substitutional defect (N_B), which generates a mid-gap state, can enhance UVC (ultraviolet C) absorption and PFCA oxidation. This work provides insight into the PFCA oxidation mechanism and reveals engineering strategies to design better photocatalysts for PFCA degradation.

KEYWORDS: *perfluorocarboxylic acids (PFCA) degradation, photoelectrochemical reactions, grand canonical density functional theory (GC-DFT), defect engineering*
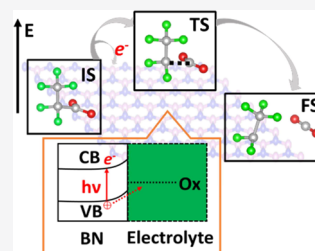
1. INTRODUCTION

Per- and polyfluoroalkyl substances (PFAS) are a variety of fluorinated organic compounds widely used in everyday products, such as food packaging, clothing, and furniture. Their high stability provides resistance to heat, oil, stains, grease, and water, but it unfortunately has an unintended consequence: PFAS accumulate in the environment and are harmful to human health.[1] PFAS have been detected in drinking water worldwide, with combined perfluorooctanesulfonic acid (PFOS) and perfluorooctanoic acid (PFOA) concentrations in many places exceeding the US EPA's lifetime health advisory of 70 ng/L.[2] Because of the strong C–F bonds in these molecules, they are persistent and hard to break down through chemical or biological processes. Effective catalytic materials for degrading PFAS to harmless substances are urgently needed.

Perfluorocarboxylic acids (PFCA, $C_nF_{2n+1}COO^-$) are a major class of PFAS contamination in drinking water, with PFOA ($C_7F_{15}COO^-$) being the most common one.[3] Among the decomposition methods that have been proposed to treat PFOA, heterogeneous photocatalytic decomposition is an attractive option because it requires relatively mild reaction conditions and can use solar energy.[1] We were recently part of a team that reported the unexpectedly high activity of hexagonal boron nitride (hBN) for photocatalytic PFOA degradation.[4]

hBN is normally considered an electrical insulator, rather than a photocatalyst, because of its wide band gap (~6.0 eV).[5] However, BN materials are now being studied to improve the photocatalytic efficiency for water splitting and water treatment.[4,6−9] Density functional theory (DFT) is one of the useful tools that have been applied to study the photocatalytic properties of hBN and design better catalysts. Wan et al.[6] applied DFT to design high-performance carbon-doped porous hBN for water treatment under visible light. Dorn et al.[10] compared experimental and DFT-calculated solid-state NMR (SSNMR) spectra to elucidate the nature of edge defects on exfoliated hBN nanosheets in solution. Weston et al.[11] studied the properties and stability of native point defects in hBN. The role of oxygen dopants in hBN for the photocatalytic degradation mechanism of CF_3COOH (the shortest member of the PFCA family) was highlighted by Salavati-fard et al. in their work using DFT.[12] In their work, a neutral simulation cell was employed, which would keep the Fermi level of the O-doped surface in the conduction band, representing the reaction condition where the electrons are excited to the

conduction band and proceed to participate in reduction reactions. However, in this work, we focus instead on the oxidation of PFCA by holes generated in the valence band of hBN. To get a deeper mechanistic insight into previous experimental observations of photo-oxidative PFCA degradation over hBN,[4] we investigated the role of photogenerated holes on hBN under a different physical situation, where the Fermi level is always kept near the edge of the valence band.

Chemical scavenger experiments in our previous work[4] demonstrated that photo-induced holes play a primary role in activating PFOA, as no degradation was observed in the presence of hole-scavenging ethylenediaminetetraacetic acid (EDTA).[4] Scavenger experiments with superoxide dismutase (SOD) and tertiary butyl alcohol (TBA) acting as superoxide anions ($^.O_2^-$) and hydroxyl radical ($^.OH$) scavengers, respectively, showed that the degradation of PFOA is slowed, but still occurs, in the absence of $^.O_2^-$ and $^.OH$. This indicates that $^.O_2^-$ and $^.OH$ facilitate, but do not initiate, the degradation mechanism.

Based on these observations,[4] we hypothesize that photogenerated holes in the valence band of hBN activate the deprotonated PFOA anion ($C_7F_{15}COO^-$) through a one-electron oxidation. Because PFCAs with different chain lengths are detected in the degradation experiment,[4] the PFOA degradation mechanism most likely proceeds in a stepwise decarboxylation cycle via a cleavage of the C—C bond.[13] Therefore, we propose that the activation of PFCA at the beginning of each cycle happens via oxidation of PFCA and the cleavage of the $-CF_2-COO^.$ bond (i.e., $C_nF_{2n+1}COO^- + h^+ \rightarrow C_nF_{2n+1}^. + CO_2$). A schematic of this oxidation reaction is shown in Figure 1a, where the initial state (IS) represents a PFCA anion ($C_nF_{2n+1}COO^-$; $n = 1–7$) approaching the hBN surface. Under illumination, holes created in the hBN valence band oxidize $C_nF_{2n+1}COO^-$ to generate an unstable perfluorocarboxyl radical ($C_nF_{2n+1}COO^.$) that rapidly dissociates in the aqueous environment, forming a perfluoroalkyl radical ($C_nF_{2n+1}^.$) and CO_2. $C_nF_{2n+1}^.$ then proceeds to degrade through established mechanisms,[4,14−21] as shown in Figure 1b. $C_nF_{2n+1}^.$ combines with $^.OH$ to form a $C_nF_{2n+1}OH$ alcohol, which then undergoes favorable HF elimination to form an unstable $C_nF_{2n}O$ fluoroaldehyde. This step is followed by hydrolysis and the formation of the next shorter-chain PFCA (i.e., $C_{n−1}F_{2(n−1)+1}COO^-$), allowing the PFCA degradation cycle to begin again.[4,14−21] Zhang et al.[22] explored this reaction sequence using DFT and demonstrated that all steps after the formation of $C_nF_{2n+1}^.$ are feasible in solution (even in the absence of a catalyst surface). Ellis et al.[23] established the mechanistic sequence of HF elimination from perfluorinated alcohols followed by hydrolysis to form shorter PFCAs. This mechanism was supported in their work by the detection of perfluorinated carboxylic acid fluorides (i.e., $C_{n−1}F_{2n−1}CFO$) during PFCA degradation by ^{19}F nuclear magnetic resonance (NMR) analysis. Zhuo et al.[24] used electrospray ionization mass spectrometry (ESI-MS) to show that the electrolysis of PFOA dissolved in $H_2(^{18}O)$ on a Ti/SnO$_2$-Sb-Bi electrode forms $C_7F_{15}(^{18}O)H$ from C_7F_{15} and $^.(^{18}O)H$, followed by the generation of $C_6F_{13}C(^{18}O)F$ after HF elimination, and then hydrolysis to produce $C_6F_{13}C(^{18}O)(^{18}O)^-$. Thus, the reaction mechanism following the formation of the perfluoroalkyl radical ($C_nF_{2n+1}^.$) is well-established in the literature. The formation of HF/F$^-$ was also detected in our previous experiments.[4] What remains uncertain in the photo-oxidative mechanism for PFCA degradation on hBN is how the initial oxidation step occurs, which is one of our focuses in this work.

Furthermore, in our previous study,[4] we observed the importance of defects within hBN for promoting its photo-catalytic activity through diffuse-reflectance UV (DR-UV) and Raman spectroscopies, and we found that ball-milling the material improved its PFOA degradation activity.[4] It was hypothesized that defects in the hBN material are necessary for its UVC light absorption and photo-degradation capability. However, we still do not know what kinds of defects are present and how they affect the PFOA degradation mechanism. In addition, previous degradation experiments[4] showed that shorter PFCA chains accumulate over time, implying that it is harder to degrade short-chain PFCAs over hBN.[4] Therefore, further investigation is needed to understand this difference in behavior among PFCAs with different chain lengths.

In this work, we apply theory to thoroughly examine previous findings and hypotheses,[4] and to answer several questions that remain unclear: Is the proposed photo-oxidation mechanism feasible? Are there any thermodynamic or kinetic limitations to the oxidation of the PFCA anion over hBN? What is the effect of structural defects present in the commercial hBN (used in the original experiments[4]) on PFOA degradation? Why do shorter-chain PFCAs degrade more slowly and accumulate in the system? Theoretical insight into these questions is critical not only for understanding the superior photocatalytic activity of hBN but also for designing better photocatalytic materials by introducing controlled surface modifications that favor the PFCA activation mechanism.

Figure 1. (a) Schematic of the key oxidation reaction $CF_3CF_2COO^- + h^+ \rightarrow CF_3CF_2^. + CO_2$ under illumination over hBN. $h\nu$ is the energy of photons required to generate photo-induced charge carriers. Under illumination, electrons are excited to the conduction band (CB), and holes are created in the valence band (VB). The holes can then oxidize reactants near the semiconductor surface based on their potential relative to the redox potential required for the oxidation reaction (Ox). (b) Proposed oxidative mechanism of the PFOA degradation reaction. Green color in the mechanism highlights the focus of this work. Atoms in Pink: B, Purple: N, Green: F, Gray: C, and Red: O

2. METHODS

Our general strategy in this work is to use DFT, as implemented in the Vienna ab initio simulation package (VASP 5.4.4),[25,26] to investigate the thermodynamic and
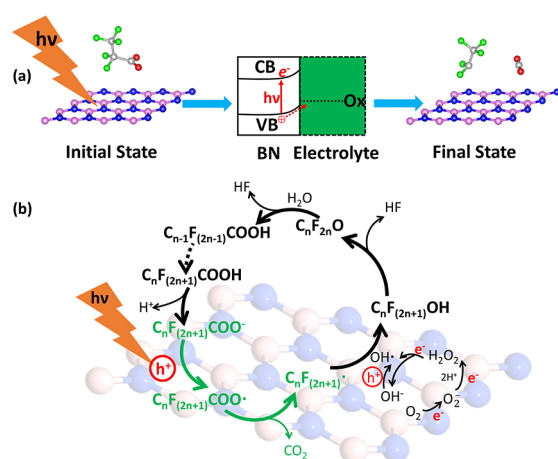
kinetic feasibility of the PFCA oxidation reaction over illuminated hBN. To determine thermodynamic feasibility, we compute the band edge alignment of hBN and compare it to the oxidation potential of PFCA, as well as calculate the reaction energy of PFCA oxidation under illumination as a function of the hBN surface charge density. To confirm the accuracy of the computed band edge alignment of hBN, we also apply ultraviolet photoelectron (UP) spectroscopy and use a Tauc plot from the DR-UV data to experimentally determine the valence band maximum (VBM) and band gap (E_g) of hBN, respectively. To determine kinetic feasibility, we calculate the activation barrier for PFCA oxidation over the illuminated hBN surface as a function of surface charge density. In addition, we applied the Marcus theory[27,28] to calculate the electron transfer rate in the PFCA oxidation reaction.

We applied an electronic grand canonical density functional theory (GC-DFT) formalism,[29−32] which was developed in our previous work[33] to study photoelectrochemical reactions on semiconductor surfaces, to calculate reaction energies and barriers as a function of variable surface charge under illumination. This approach allows one to model chemical reactions under constant illumination or applied potential, which is difficult in the usual canonical DFT formalism because the work function of the electrode surface changes significantly during the electron transfer reaction.[25,26] In this approach, we control the surface charge density by changing the total electron number in the system to match the desired potential of the semiconductor. The VASPsol implicit solvation scheme maintains charge neutrality in the simulation cell by placing implicit counterions in the electrolyte to screen charged species.[34,35] For each reaction energy or kinetic barrier reported here, the initial state (IS), transition state (TS), and final state (FS) have the same number of electrons in their respective unit cells, but electron transfer takes place between the surface and the PFCA molecule during the reaction. This induces a change in the hBN surface charge density, which is influenced by the size of the photocatalyst surface model. For this reason, we applied models with increasing cell size (4×4, 6×6, and 8×8 hBN) to extrapolate the energetics to those of an infinite surface model. In this limit, the change in surface charge density during the reaction is negligible, allowing us to determine the converged reaction energetics at a constant surface charge density.

After establishing the behavior of the pristine hBN material, we investigate the effect of defects present in commercial hBN. We apply X-ray photoelectron spectroscopy (XPS) to characterize the composition and nature of defects present in the material and then use DFT to assess how these defects can affect the PFCA degradation mechanism. The DFT settings, the calculation details, and the experimental method are discussed in detail in the Supporting Information (SI).

3. RESULTS AND DISCUSSION

3.1. hBN VB Edge Position versus PFCA Oxidation Potential.
We first examine the thermodynamic favorability of PFCA oxidation by comparing the computed PFCA oxidation potential to the VBM of hBN (Figure 2a−c). A reaction with a less positive oxidation potential than the VBM position (i.e., an oxidation potential above the VBM position on the band diagram in Figure 2) is exergonic. We calculate the oxidation potential referenced to the standard hydrogen electrode (SHE)[36] for both the formation of a perfluorocarboxyl radical (i.e., $CF_3CF_2COO^-_{(aq)} + h^+ \rightarrow CF_3CF_2COO^._{(aq)}$, black solid
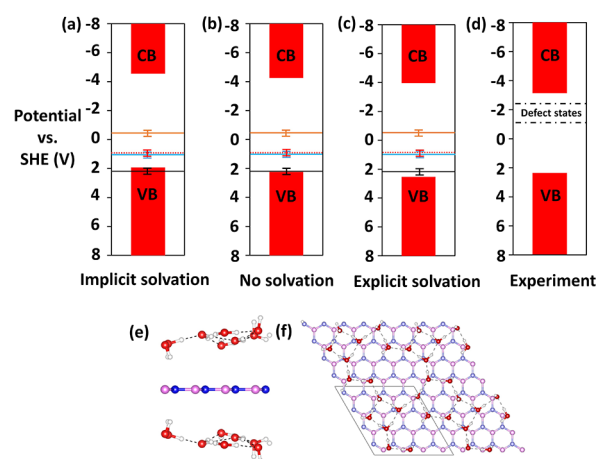
Figure 2. Calculated redox potentials for the reactions: $CF_3CF_2COO^-_{(aq)} + h^+ \rightarrow CF_3CF_2COO^._{(aq)}$ (black solid horizontal lines), $CF_3CF_2COO^-_{(aq)} + h^+ \rightarrow CF_3CF_2^._{(aq)} + CO_{2(g)}$ (blue solid horizontal lines), $OH^-_{(aq)} + h^+ \rightarrow ^.OH_{(aq)}$, (red dotted line), and $O_{2(aq)} + e^- \rightarrow ^.O_2^-_{(aq)}$ (orange solid line) and their positions relative to the band edge alignment of a 4×4 hBN surface that is (a) implicitly solvated, (b) in vacuum (no solvation), and (c) explicitly solvated. An RMSE error bar of 0.2 V is depicted on the redox potential of all the reactions to reflect the error associated with the redox potential calculations, as benchmarked in the Supporting Information. (d) Band diagram of hBN measured via experiment. The black dotted line shows the approximated range of defect states. (e) Side view of the explicitly solvated 4×4 hBN surface model. (f) Top view of the network of water molecules formed in the explicitly solvated system. The gray cell shows the size of one 4×4 surface model. Atoms in Red: O, white: H, Pink: B, Purple: N

horizontal line in Figure 2a−c) and the simultaneous formation of a perfluoralkyl radical and carbon dioxide (i.e, $CF_3CF_2COO^-_{(aq)} + h^+ \rightarrow CF_3CF_2^._{(aq)} + CO_{2(g)}$, blue solid horizontal line in Figure 2a−c). The calculation details for computing standard redox potentials are discussed in the Supporting Information. The results show that a much more positive potential is required to form the perfluorocarboxyl radical (2.18 V_{SHE}) compared to the perfluoroalkyl radical and CO_2 (1.15 V_{SHE}). This indicates that the dissociation of the perfluorocarboxyl radical ($CF_3CF_2COO^.$) into the perfluoroalkyl radical ($CF_3CF_2^.$) and CO_2 is favorable. The redox potential of $CF_3CF_2COO^-_{(aq)} + h^+ \rightarrow CF_3CF_2COO^._{(aq)}$ lies close to the VBM of hBN when the system is treated with or without implicit solvation (the black solid line in Figure 2a,b, respectively), with the difference falling within the simulation RMSE of ± 0.2 V (Figure S3). This suggests that the oxidation of PFCA by a photogenerated hole on hBN is thermodynamically feasible. We also calculate the band edge alignment with one explicit water layer added to each side of the hBN model (Figure 2e,f) and find that the VBM of explicitly solvated hBN lies at a more positive position than the PFCA oxidation potential (Figure 2c). This further confirms the thermodynamic feasibility of PFCA oxidation from the aspect of band edge alignment. In addition, the generation of $^.OH$ and $^.O_2^-$ from the oxidation of OH^- and reduction of O_2, respectively, is also favorable, given the band edges of hBN, which straddle the calculated oxidation potential of OH^- (E^0 ($^.OH/OH^-$) = 1.12 V_{SHE}, red dotted line in Figure 2a−c) and the calculated reduction potential of O_2 (E^0 ($O_2/^.O_2^-$) = −0.51 V_{SHE}, orange solid line in Figure 2a−c). $^.OH$ also could be generated by a series of thermodynamically favorable reduction reactions[37] of
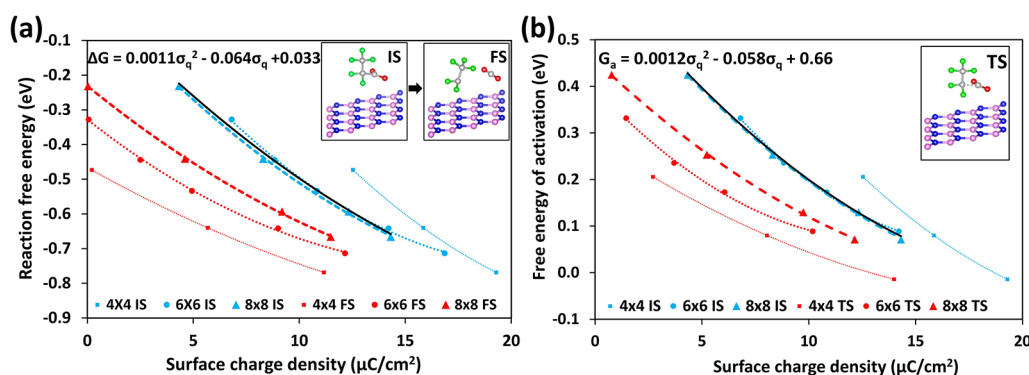
Figure 3. (a) Reaction free energy of $CF_3CF_2COO^-_{(aq)} + h^+ \rightarrow CF_3CF_2^{\cdot}{}_{(aq)} + CO_{2(aq)}$ as a function of surface charge density of the IS and FS over 4×4, 6×6, and 8×8 simulation unit cells. The blue dotted lines represent the reaction energy as a function of IS surface charge density, and the red dotted lines refer to the reaction energy as a function of FS surface charge density. A thicker line represents a larger simulation cell. The relationship between the reaction energy (ΔG) and the IS surface charge density (σ_q) is predicted by fitting a quadratic polynomial (the black solid line) using the data from both 6×6 and 8×8 systems within the range of σ_q from 5 to 15 μC cm^{-2}. The insets show the geometries of the IS and FS. (b) Free energy of activation of the reaction $CF_3CF_2COO^-_{(aq)} + h^+ \rightarrow CF_3CF_2^{\cdot}{}_{(aq)} + CO_{2(aq)}$ as a function of the surface charge density of the IS and TS over 4×4, 6×6, and 8×8 unit cells. The relationship between the activation energy (G_a) and IS surface charge density (σ_q) is predicted by fitting a quadratic polynomial (the black solid line) using the data from both 6×6 and 8×8 systems within the range of σ_q from 5 to 15 $\mu C/cm^2$. The inset shows the structure of the TS in a 4×4 system. Atoms in pink: B, purple: N, green: F, gray: C, and red: O.

$^{\cdot}O_2^-$ over hBN (i.e., $^{\cdot}O_2^- + e^- + 2H^+ \rightarrow H_2O_2$, E^0 ($^{\cdot}O_2^-/H_2O_2$) = 0.93 V_{SHE}, pH = 7;[37,38] $H_2O_2 + e^- \rightarrow {}^{\cdot}OH + OH^-$, E^0 ($H_2O_2/{}^{\cdot}OH$) = 0.30 V_{SHE}, pH = 7[37,38]). Thus, all these species would be available under illumination to complete the reaction mechanism shown in Figure 1b. The experimentally measured hBN band diagram (especially the VBM, which matters in determining the thermodynamic favorability of the oxidation reactions) compares well with our calculation result (Figure 2d). The details of the experiment are described in the Supporting Information (Figure S5). A similar method can be used to assess the hBN photo-degradation performance for other PFAS, such as PFOS and GenX [ammonium perfluoro-(2-methyl-3-oxahexanoate)], and a detailed discussion is provided in the Supporting Information. (Figure S6).

3.2. Explicit Calculation of PFCA Oxidation Energy and Barrier over hBN. Although we have proved the thermodynamic favorability of PFCA oxidation after hBN is photoexcited and holes are generated, the VBM of hBN can change based on surface charge density, and a more rigorous way to determine the reaction feasibility is to include the hBN surface in the simulation model when calculating the reaction energy and the activation barrier over the catalyst surface explicitly. Therefore, we further confirm the thermodynamic favorability of PFCA oxidation by computing the explicit reaction free energy for PFCA oxidation reaction on hBN (Figure 3a). Applying the same GC-DFT formalism from our previous work[33] on a 4×4 hBN cell (the rightmost blue dotted line in Figure 3a), we find that the PFCA oxidation reaction to form a perfluoralkyl radical and CO_2 is favorable for positive surface charge densities higher than 12.5 μC cm^{-2} in the IS (this IS surface charge density corresponds to the presence of one hole on the 4×4 hBN surface). The oxidation reaction becomes more favorable when the surface charge density is increased as more holes are present on hBN. The reaction is unfavorable in the absence of a hole on hBN (1.61 eV), as the excess electron in the PFCA anion ($-1.0 \ e$) is not transferred to the hBN surface, resulting in the formation of the unstable $CF_3CF_2^-$ species in the FS. This is further evident from the comparison of the density of states (DOS) of neutral hBN surface before (IS) and after the reaction (FS) shown in

Figure S7, which demonstrates that the Fermi level (taken herein to mean the energy of the highest occupied state) increases from the VBM in the IS to a high-energy mid-gap level generated by the under-coordinated $CF_3CF_2^-$ species in the FS. Intuitively, this underscores the importance of photo-induced holes on hBN for driving PFCA oxidation.

The size of the simulation cell influences the change in the surface charge density that occurs when a fixed number of electrons is transferred to the surface during the PFCA oxidation reaction. We model the oxidation reaction on larger 6×6 and 8×8 cells to investigate the effect of the simulation cell size and to obtain size-converged reaction energies. Extrapolation to an infinite surface model represents the limit where the surface charge density remains unchanged during the reaction, which is more representative of the large experimental system. We plot the overall oxidation reaction free energy as a function of the IS and FS surface charge densities for 4×4, 6×6, and 8×8 simulation cells in Figure 3a. As expected, the relationship between the reaction energy and the surface charge density in the larger simulation cell has the same trend as in the 4×4 cell. The change in the surface charge density from IS to FS during the reaction (i.e., the horizontal distance between the IS curve and the FS curve in Figure 3a) decreases with increasing unit cell size. We also find that the dependence of the reaction energy on surface charge density varies more with respect to changes in the FS cell sizes compared to the IS cell sizes. For 6×6 and 8×8 cells, the reaction energies merge with respect to IS surface charge densities. Therefore, we can use the merged data to predict the reaction energy as a function of IS surface charge density to extract the infinite surface limit. The relationship between the reaction free energy (ΔG) and the IS surface charge density (σ_q) is obtained by fitting a quadratic polynomial within the range of σ_q from 5 to 15 μC cm^{-2} yielding $\Delta G = 0.0011\sigma_q^2 - 0.064\sigma_q + 0.033$. This range of surface charge density is physically consistent with experiments,[39,40] where the surface charge density reported for BN nanoporous membranes and transmembrane BN nanotubes has a magnitude between 7 and 16 μC cm^{-2}.

The dependence of the reaction energy on the IS charge density is explained based on the position of the Fermi level in cells with different sizes in the Supporting Information (Figure S8). The convergence of the reaction energy with respect to the cell size is similar to what was found in our previous work[33] investigating the HER reaction, where we found that reaction energy computed as a function of the FS surface charge density converged quickly.

Next, we calculate the activation barrier to investigate the kinetic favorability of PFCA oxidation over hBN as a function of the surface charge density (Figure 3b). The reaction barrier is always less than 0.5 eV for the relevant surface charge densities sampled on all three cell sizes. As expected, the activation energy decreases with increasing surface charge density. Similar to the reaction free energy results, we find that the activation energy as a function of IS surface charge density converges with respect to the cell size in the 6×6 and 8×8 surface models. Therefore, using the converged data, we fit a quadratic polynomial to compute the infinite-cell reaction barrier as a function of the IS surface charge density: $G_a = 0.0012\sigma_q^2 - 0.058\sigma_q + 0.66$. The activation energy decreases from 0.45 to 0.11 eV as the surface charge density increases from 5 to 15 μC cm^{-2}. These barriers are surmountable at room temperature,[41] demonstrating that the one-electron oxidation step is viable for PFCA activation.

We analyze the IS, TS, and FS in a neutral 6×6 system to better understand the nature of the electron transfer process as the PFCA is oxidized. Although the overall unit cell is neutral, there is spontaneous charge separation between the molecules and the surface (Figure S9). In the IS, the surface is positively charged ($+0.84$ e, 6.8 μC cm^{-2}) and the molecule is negatively charged (-0.84 e). The surface charge density approaches zero in the TS and FS (1.5 and 0.07 μC cm^{-2}, respectively), showing that the hBN surface accepts an electron from the molecule during the reaction (Figure 4a–c). The DOS of each state in Figure 4d–f shows that the Fermi level shifts to a

higher energy going from the IS to the FS, showing that electrons are transferred to the hBN surface during the reaction. The surface charge density and the Fermi level of the TS are much closer to those in the FS than those in the IS, meaning that most of the electrons have been transferred from the molecule to the hBN surface before the TS geometry is attained. The length of the C−C bond that breaks in the process is 1.55, 1.93, and 4.28 Å in the IS, TS, and FS, respectively (Figure 4a–c). This suggests that charge transfer precedes the scission of the C−C bond and that the TS closely resembles the $CF_3CF_2COO^{\cdot}$ radical. We also simulate the dissociation of this radical (i.e., $CF_3CF_2COO^{\cdot}{}_{(aq)} \rightarrow CF_3CF_2{}^{\cdot}{}_{(aq)} + CO_{2(aq)}$) in the absence of the hBN surface. The reaction is favorable by -1.4 eV and is barrierless, in agreement with values computed by Zhang et al.[22] for this reaction using the M06-2X functional with SMD solvation. This suggests that the $CF_3CF_2COO^{\cdot}$ radical will dissociate rapidly once the electron is transferred to the surface. Thus, hBN plays an important role in facilitating PFCA oxidation by extracting an electron from the PFCA anion, forming a radical that undergoes spontaneous dissociation. Therefore, we conclude that the PFCA oxidation mechanism consists of two steps: (1) an electron transfers from $CF_3CF_2COO^{-}$ to fill a hole present in the hBN VB and (2) the $CF_3CF_2COO^{\cdot}$ rapidly dissociates to $CF_3CF_2{}^{\cdot}$ and CO_2. We applied Marcus theory[27,28] (Figure S10) to calculate the electron transfer rate of the outer-sphere electron transfer reaction: $CF_3CF_2COO^{-}{}_{(aq)} + *(+1\ e) \rightarrow CF_3CF_2COO^{\cdot}{}_{(aq)} + *(0\ e)$, where * represents the 4×4 hBN surface in the aqueous environment. We found that the electron transfer rate is 7.70×10^6 s^{-1} (full calculation details are described in the Supporting Information), demonstrating that electron transfer is fast. Despite a distance of ~4.0 Å between the head group of PFCA and the hBN surface, the electronic coupling between the two is strong (i.e., 0.004 eV) because the redox potential of $CF_3CF_2COO^{-}{}_{(aq)} + h^{+} \rightarrow CF_3CF_2COO^{\cdot}{}_{(aq)}$ lies close to the VBM of hBN (Figure 2), which allows states in the VB band edge to couple strongly to the highest occupied molecular orbital (HOMO) of the PFCA. This strong coupling, combined with a small reorganization energy, yield rapid electron transfer between the PFCA anion and available VB states in the hBN.

To better understand the characteristics of holes generated on hBN, we also analyzed the partial DOS (PDOS) shown in Figure S11 and found that the states at the VB edge of hBN are mainly contributed by 2p orbitals of N atoms. This suggests that the photogenerated holes would be delocalized across the N atoms of hBN.

Having understood the oxidative degradation mechanism, we next aim to examine why short-chain PFCAs do not degrade efficiently in the experiments.[4] First, we compute the oxidation potentials of PFCA anions with various chain lengths. We find that the oxidation potentials do not depend significantly on the PFCA chain length (Figure 5a). Therefore, the feasibility of the oxidation reaction step is not affected by the chain length, and therefore, our choice of investigating a short-chain PFCA is well justified in terms of the significant reduction in computational expense. As the oxidation feasibility does not explain the lower efficiency of hBN to degrade short-chain PFCA, we investigate the adsorption of PFCA with varying chain lengths on the hBN surface. Because the PFCA oxidation reaction is a surface reaction with adsorption being the first step of the PFCA degradation
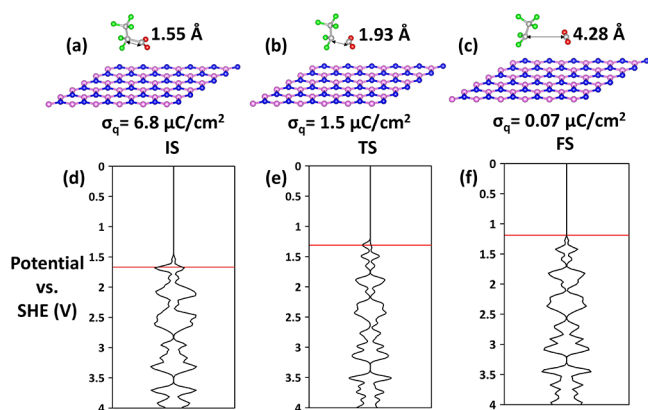

Figure 4. Structure of (a) IS, (b) TS, and (c) FS of the oxidation reaction in a 6×6 neutral system. The length of the C−C bond that breaks in the reaction and the hBN surface charge density are listed in the figure, showing structural change and charge transfer during the oxidation reaction: $CF_3CF_2COO^{-}{}_{(aq)} + h^{+} \rightarrow CF_3CF_2{}^{\cdot}{}_{(aq)} + CO_{2(aq)}$. Atoms in pink: B, purple: N, green: F, gray: C, and red: O. The DOS near the VB edge of (d) IS, (e) TS, and (f) FS of the overall oxidation reaction in a neutral 6×6 system. The vertical axis has units of V and is referenced to SHE, and the DOS on the horizontal axis has the units of states eV^{-1} $cell^{-1}$. The horizontal red solid line represents the position of the Fermi level.
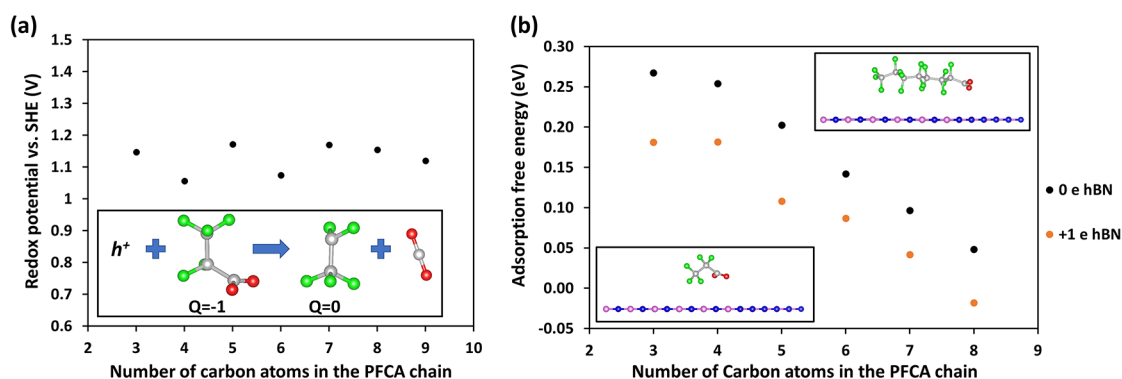
Figure 5. (a) Calculated redox potential of the oxidation reaction: $C_nF_{2n+1}COO^-_{(aq)} + h^+ \rightarrow C_nF_{2n+1}^{\cdot}{}_{(aq)} + CO_{2(g)}$ as a function of the PFCA chain length. The inset shows the oxidation of $C_3F_5COO^-$. (b) The adsorption free energy of PFCA anions with different chain lengths on 6×6 pristine hBN (charge $0\ e$) and 6×6 pristine hBN (charge $+1\ e$) in a parallel binding mode. The insets show the adsorption configuration of $C_3F_5COO^-$ and $C_8F_{15}COO^-$. Atoms in pink: B, purple: N, green: F, gray: C, red: O, and white: H.
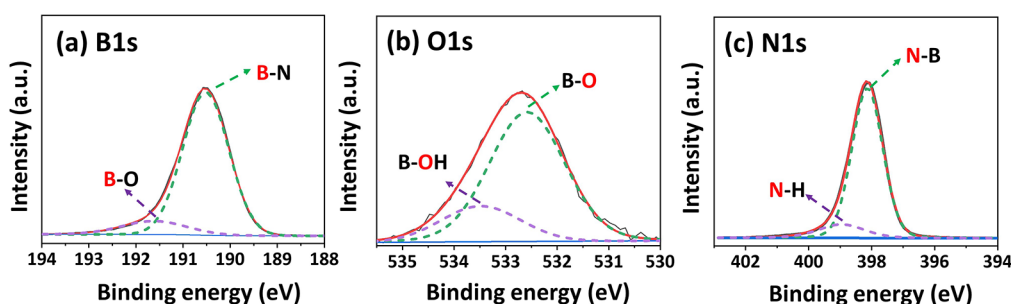

Figure 6. (a) B1s, (b) O1s, and (c) N1s XPS spectra of commercial hBN. The black solid lines represent the obtained spectra from the XPS experiments. The fitted spectra are shown in the red solid lines. The spectra deconvolution results are displayed in the purple and green dotted lines.

mechanism, the weak adsorption of reactants on the photo-catalyst can impede the following photo-oxidation step. We find that PFCA prefers to bind parallel to the hBN surface compared to binding in a perpendicular fashion (Figure S12). Because the main interaction between the PFCA (with charge $-1\ e$) and the neutral hBN ($0\ e$) surface is van der Waals (vdW), the parallel binding mode (with a greater total area of interaction) is more favorable compared to the perpendicular binding mode (via the head group). Similarly, the adsorption of shorter-chain PFCA on hBN is less favorable because of the weaker vdW interaction, as shown in Figure 5b. When hBN is under illumination and is positively charged ($+1\ e$), the adsorption of the PFOA anion would be more favorable because of the additional electrostatic interaction (shown as orange data in Figure 5b). Thus, inducing positive charge on the hBN surface can be an effective way to enhance the degradation of short-chain PFCAs. We also tested the adsorption of PFCA on the defects we identified in the following section and found that the adsorption is not affected much by the defects (Figure S13).

From the previous discussion, we found that hBN is an extraordinary photocatalyst for PFCA degradation for several reasons. First, the hydrophobicity of hBN enhances the adsorption of the PFCA with long hydrophobic, fluorine-saturated carbon-chain on the catalyst surface. Second, the VBM of hBN lies at a more positive position than the PFCA oxidation potential (Figure 2). This confirms the thermodynamic feasibility of PFCA oxidation from the aspect of the band edge alignment. Third, the HOMO of PFCA lies close to the VBM of hBN, yielding significant overlap of the donor and

acceptor wavefunctions that promotes strong coupling that increases the probability of electron transfer.

3.3. Influence of Defects on hBN Photocatalytic Performance. The oxidative activation of PFCA by illuminated hBN is exergonic with a surmountable barrier under room temperature. However, the band gap of pristine hBN (6.08 eV[5]) is too large to be illuminated under the 254 nm UVC light[4] (4.88 eV). Our original PFOA degradation experiments employed a defective hBN material and suggested the importance of surface defects for UVC adsorption and photocatalytic activity of the hBN material.[4] For simplicity, we used a pristine hBN surface for our theoretical calculations presented above, while the experiments were carried out with commercial hBN containing various defects. Therefore, it is essential to understand how the results of our calculations would be affected by the presence of the defects, which include point defects and edges, on hBN. According to the theoretical study reported by Weston et al.,[11] nitrogen-at-boron-site substitutions (N_B) and oxygen-at-nitrogen-site substitutions (O_N) are the most stable point defects under N-rich conditions when the Fermi level is close to the VBM, which is the case under the oxidizing conditions in our experiments. Besides point defects, two kinds of edge defect configurations, that is, zigzag (alternating B and N terminated edges) and armchair (edges with alternating B and N atoms), might be present in hBN and affect the photocatalytic process.[10,42,43] Dorn et al.[10] compared the experimental and DFT-calculated solid-state NMR (SSNMR) spectra and confirmed that both armchair and zigzag edge termination are present on exfoliated hBN nanosheets in aqueous solution. Therefore, we also consider
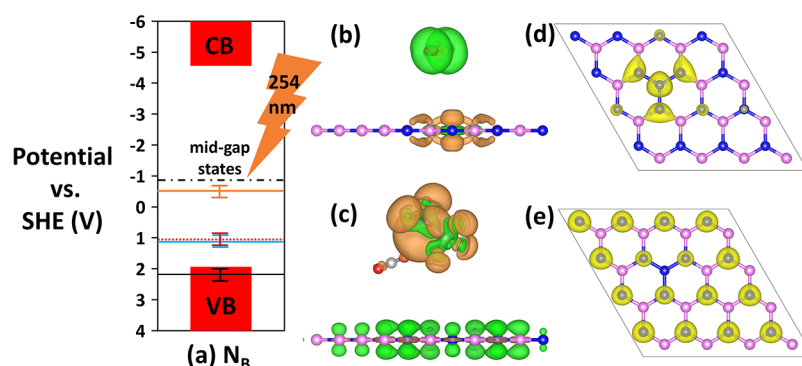
Figure 7. (a) Calculated redox potentials for the reactions: $CF_3CF_2COO^-_{(aq)} + h^+ \rightarrow CF_3CF_2COO^._{(aq)}$ (black solid horizontal line), $CF_3CF_2COO^-_{(aq)} + h^+ \rightarrow CF_3CF_2^._{(aq)} + CO_{2(g)}$ (blue solid horizontal line), $OH^-_{(aq)} + h^+ \rightarrow ^.OH_{(aq)}$, (red dotted line), and $O_{2(aq)} + e^- \rightarrow ^.O_2^-_{(aq)}$ (orange solid line) and their positions relative to the band edge alignment of a 4×4 N_B defective hBN surface that is implicitly solvated. The black dotted line shows the position of the mid-gap states generated by N_B defects. An RMSE error bar of 0.2 V is depicted on the redox potential of all the reactions to reflect the error associated with the redox potential calculations, as benchmarked in the Supporting Information. The potential on the vertical axis has the units of V and is referenced to SHE. Electron density difference plots of adsorbed (b) O_2 on a neutral 4×4 N_B defective hBN surface and (c) $CF_3CF_2COO^-$ on a 4×4 illuminated N_B defective hBN surface (charge state: $+3$ e). The orange isosurface represents electron density depletion (positively charged) and the green isosurface represents electron density accumulation (negatively charged). The isosurface level of charge accumulation and depletion is 0.01 e Å^{-3}. Top view of the orbital image of the (d) mid-gap states (potential range -1.46 V_{SHE} to -0.79 V_{SHE} from Figure S14c) and (e) VB edge (potential range from 1.19 to 2.05 V_{SHE} from Figure S14c) in a 4×4 neutral N_B defective system. An isovalue of 0.03 e Å^{-3} was used to generate the yellow isosurfaces of the electron density. Atoms in pink: B, purple: N, green: F, gray: C, and red: O.

PFCA oxidation in the vicinity of zigzag and armchair edges of hBN in this work.

We apply XPS to confirm the type of point and edge defects present in the commercial hBN samples (used in our previous experiments[4]). The deconvoluted B1s spectrum of hBN (Figure 6a) shows peaks that are indicative of the B−N (190.5 eV) and B−O (191.7 eV) bonds.[44,45] In the deconvoluted O1s XPS spectrum (Figure 6b), B−O (532.5 eV)[46] and B−OH (533.4 eV)[47] bonds are also observed. The existence of B−OH and B−O bonds suggests that the commercial BN material has B−OH/B−O termination at the edges. The B−O bonds might also correspond to oxygen substitution defects at nitrogen sites (O_N), so both B−O bond formation as edges and point defects are considered in our models. Peaks of N−B (398.1 eV) and N−H (399.0 eV) bonds[48] are found in the N1s peak deconvolution results (Figure 6c), suggesting the existence of an edge with N−H termination in the commercial hBN as well. The average atomic composition of the commercial hBN was determined to be 45.4 ± 0.3% B, 50.5 ± 0.2% N, and 4.1 ± 0.1% O, where a higher content of N suggests the existence of N_B defects in the commercial hBN. Thus, both our XPS data and the stability analysis reported by Weston et al.[11] indicate that O_N and N_B defects likely are present in the commercial hBN. Also, the XPS spectra suggest the existence of B−OH, B−O, and N−H groups at the edge of commercial hBN, which is consistent with the edge termination characterized by Dorn et al.[10]

We study the DOS of the 4×4 pristine hBN surface and the 4×4 defective hBN surface models with one O_N or N_B defect to understand how these defects might affect the oxidation of PFCA (Figure S14a−c). The Fermi level lies in the CB for the neutral O_N surface (Figure S14b) and at a mid-gap state for the neutral N_B surface (Figure S14c). The neutral defects will not be stable in the aqueous electrolyte because the reduction potentials of O_2/H_2O (1.23 V_{SHE}[49]) and $O_2/^.O_2^-$ (-0.51 V_{SHE}) fall below the Fermi level of neutral O_N and N_B defective surfaces shown in Figure S14b,c. Electrons occupying the high-energy CB or mid-gap states in the neutral defective systems

would spontaneously flow into the aqueous electrolyte. Thus, these defects will exist in a positive charge state with the Fermi level shifted to the VBM position.

For hBN with O_N defects, the band edges, in particular the VBM, (Figure S14b) are almost the same as those of pristine hBN (Figure S14a), which suggests that the O_N impurities would not affect the light absorption or the PFCA degradation mechanism. The N_B defect also has a negligible effect on the position of the VBM (Figure S14c), so the thermodynamic feasibility of PFCA oxidation will not be affected. N_B generates mid-gap states that enable the absorption of UVC light, which otherwise is impossible in a large band gap semiconductor like hBN. The energy gap between the mid-gap states and VBM is 2.8 eV for the N_B surface (Figure S14c), which is lower than the energy of 254 nm UVC light (4.88 eV). We computed the band edge alignment of the N_B defective hBN surface and compared it with the redox potentials of the key reactions in the reaction mechanism (Figure 7a). The VMB is the same as that of pristine hBN (Figure 2a), and the position of the mid-gap state (2.8 eV above VBM) was determined from the DOS of the N_B defective hBN surface (Figure S14c). The energy level of the mid-gap state generated by the N_B defects lies above the reduction potential of $O_2/^.O_2^-$ (-0.51 V_{SHE}) (orange solid line in Figure 7a), and therefore, it is still feasible to generate $^.O_2^-$ to facilitate the PFCA degradation mechanism after the oxidation step (Figure 1b).

We conducted an additional DFT calculation to confirm that $^.O_2^-$ can be generated through electron transfer from the mid-gap state to O_2, wherein we relaxed a O_2/hBN-N_B geometry and analyzed the redistribution of charge when O_2 approaches the surface (for efficiency, the Perdew−Burke−Ernzerhof (PBE)[50] functional was used to relax the geometry, and the strongly constrained and appropriately normed (SCAN)[51] functional was used to compute the charge distribution in the relaxed geometry). When O_2 (0 e) is placed near a neutral N_B defect in the hBN system, charge is transferred from the N_B defect to the O_2 molecule (-0.4 e) (Figure 7b). We also confirmed that holes from illuminated hBN with N_B defects
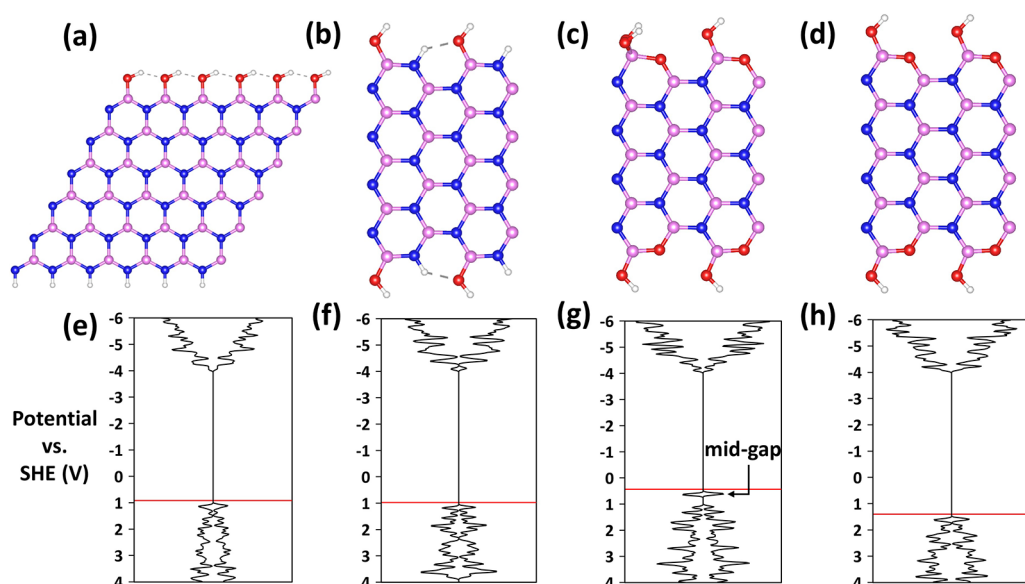
Figure 8. (a) Structure of the hBN zigzag edge with N−H and B−OH termination in a charge-neutral state. The structures of the hBN armchair edge (b) with N−H and B−OH termination in the charge-neutral state, (c) with both 3-coordinated B (B−N, B−O, and B−OH) and 4-coordinated B (B−N, B−O, and 2 × B−OH) in the −1 e charged state (to account for the negatively charged 4-coordinated boron species), and (d) with only 3-coordinated B (B−N, B−O, and B−OH) in the charge-neutral state. Respective DOS of these surfaces are shown in (e), (f), (g), and (h) below each structure. The mid-gap states associated with the adsorbed hydroxide on the 4-coordinated boron site are noted in (g). The potential on the vertical axis has the units of V and is referenced to SHE, and the DOS on the horizontal axis has the units of states eV^{-1} $cell^{-1}$. The horizontal red solid line represents the position of the Fermi level. Atoms in pink: B, purple: N, red: O, and white: H.

can oxidize $CF_3CF_2COO^-$ (Figure 7c). The initial charge state of the 4 × 4 N_B defect is +3 e to simulate the illuminated defective hBN surface where one photoexcited hole is present in the VB. When $CF_3CF_2COO^-$ (−1 e) approaches the illuminated N_B surface, the electron from the anion is transferred to the N_B surface spontaneously, followed by the C−C bond scission to generate $CF_3CF_2^{\cdot}$ (0 e) and CO_2 (0 e). (Figure 7c) The charge state of the N_B surface changes to +2 e after electron transfer. The feasibility of the reaction shows that N_B defects do not interfere with the photo-oxidative degradation mechanism of PFCA.

The mid-gap states generated by N_B defects also are beneficial for charge separation, as the mid-gap states are localized on the N_B defects (Figure 7d) and holes in the VBM are delocalized on the N atoms of the entire hBN surface (Figure 7e). Thus, the recombination rate of the photoexcited electrons and photogenerated holes would decrease in the presence of N_B defects which trap electrons.[52] Therefore, we conclude that the N_B defect enhances photo-excitation in the UVC region, as well as promotes charge separation, without interfering with the oxidation of the PFCA molecule. Introducing N_B defects would be a promising direction for improving hBN catalysts.

We also examine the DOS of other possible point defects, such as boron-at-nitrogen-site substitutions (B_N), nitrogen vacancies (V_N), and boron vacancies (V_B)[11] (Figure S14d−f). B_N and V_B surfaces have VBM positions higher than that of pristine hBN (Figure S14a), which would make oxidation to a perfluorocarboxyl radical (i.e., $CF_3CF_2COO^-_{(aq)}$ + h^+ → $CF_3CF_2COO^{\cdot}_{(aq)}$) unfavorable. Similar to the N_B defective hBN, the V_N defective hBN has the same VBM as the pristine hBN, and it also generates mid-gap states (3.3 eV above VBM). Therefore, introducing V_N defects would also help with UVC light absorption (4.88 eV) and charge carrier separation,

and thus can improve the photocatalytic activity of hBN without interfering with PFCA oxidation.

Finally, we examine how the edge defects of hBN would affect the PFCA oxidation. We chose our edge models based on our XPS results reported above and the edge terminations of solvated hBN reported by Dorn et al.[10] Both the zigzag and armchair edges of hBN were investigated. For the zigzag edge saturated by the N−H and B−OH groups (Figure 8a), the DOS (Figure 8e) is almost the same as that of pristine hBN (Figure S14a), which indicates that the band edge alignment of hBN would not be affected by the zigzag edge termination. For the armchair configuration, two molecular edge terminations were considered, that is, a N−H and B−OH termination (Figure 8b), as well as a three- and four-coordinate B−OH and B−O termination (Figure 8c). From the DOS of the edge with a N−H and B−OH termination (Figure 8f), the band edge positions are also close to those of the pristine hBN surface (Figure S14a). This suggests that the thermodynamic favorability of PFCA oxidation would also not be affected by the presence of the N−H and B−OH terminated armchair edges in the commercial hBN material. For the edge with a four-coordinate boron featuring B−N, B−O, and 2 × B−OH coordinations (Figure 8c), the VBM (Figure 8g) also is similar to that of the pristine hBN surface (Figure S14a), where mid-gap states are generated by the extra OH^- group at the four-coordinate B site (Figure S15). However, the extra *OH^- group is readily oxidized to form $^{\cdot}OH$ by holes generated under illumination, leading to the three-coordinate B site on the surface (Figure 8d). We confirm this by computing the oxidation potential to form $^{\cdot}OH$ from the four-coordinated B−OH site (i.e., *OH^- + h^+ → $^{\cdot}OH$ + *), which is 0.89 V_{SHE} (see the Supporting Information for calculation details) and lies above the VBM shown in Figure 8g. Thus, it is thermodynamically favorable for *OH^- to be oxidized by holes at the armchair edge of hBN, which could be another source of $^{\cdot}OH$

in the PFCA degradation mechanism. After the oxidation of *OH, the three-coordinate B termination shown in Figure 8d is formed, which has a VBM lower in energy (Figure 8h) than that of the pristine hBN (Figure S14a). Therefore, the presence of the B−OH and B−O terminated armchair edge would not interfere with PFCA oxidation.

Overall, XPS experiments demonstrate the presence of edge and point defects (i.e., N_B and O_N) in the commercial hBN. We determined that the O_N point defect, zigzag and armchair edge defects do not interfere with the favorability of PFCA oxidation. N_B and V_N point defects generate mid-gap states that facilitate photo-excitation under UVC and promote charge separation without interfering with the PFOA oxidation reaction step. Thus, we predict that the performance of hBN for photocatalytically degrading PFCAs can be maximized by intentionally introducing N_B and V_N defects. Structural defects can be introduced in synthesis or subsequent treatment.[53] Numerous methods have been employed to induce point defects in hBN, such as electron beam irradiation, solvent exfoliation, ball-milling, N_2 plasma treatment, heat treatment, etching, and other methods.[9,53−55] Our previous work found that ball-milling can improve the photocatalytic performance of hBN on PFOA degradation.[4] Fu et al.[9] reported that V_N defects are introduced by the ball-milling process and the activity of TiO_2/hBN composites is also enhanced by ball-milling. Ball-milling has been widely applied in industry to grind materials to increase solid-state chemical reactivity.[56] Weston et al.[11] found N_B defects, which already are present in commercial hBN materials, to be more stable when the material is synthesized under N-rich conditions. Chemical vapor deposition also may be a good way to introduce more N in the material during synthesis and has been used to dope various atoms (i.e., O, C, H, and so forth) in hBN.[53] Therefore, it is practical at scale to produce hBN with V_N and N_B defects to achieve better photocatalytic properties.

■ ASSOCIATED CONTENT

Ⓢ Supporting Information
The Supporting Information is available free of charge at https://pubs.acs.org/doi/10.1021/acs.est.2c01637.

> Details of the computational and experimental methods. Calculation details of band edge positions, reaction free energies, activation barriers, standard redox potentials, electron transfer rate using Marcus theory, and adsorption free energy; accuracy test for various XC functionals and VASPsol for calculating redox potentials; experimental spectra for band diagram measurement; tests for investigating the feasibility of GenX and PFOS oxidation on hBN; DOS of IS and FS of the oxidation reaction in the absence of holes on hBN; explanation for the dependence of the reaction energy on the IS surface charge density; DOS of IS and FS on charged 4 × 4, 6 × 6, and 8 × 8 surfaces at a certain reaction energy; charge separation in IS, TS, and FS; PDOS of hBN; DOS of pristine hBN, and defective hBN with O_N, N_B, B_N, V_N, and V_B point defects; PFCA adsorption configuration and the corresponding adsorption free energy on pristine and defective hBN surfaces; and orbital image of mid-gap states generated by the hBN armchair edge with three- and four-coordinated B−OH and B−O termination. (PDF)

■ AUTHOR INFORMATION

Corresponding Author
Thomas P. Senftle − *Department of Chemical and Biomolecular Engineering, Rice University, Houston, Texas 77005-1892, United States; Nanosystems Engineering Research Center for Nanotechnology-Enabled Water Treatment, Houston, Texas 77005, United States;* ⓞ orcid.org/0000-0002-5889-5009; Phone: +1-713-348-4714; Email: tsenftle@rice.edu

Authors
Yu Chen − *Department of Chemical and Biomolecular Engineering, Rice University, Houston, Texas 77005-1892, United States; Nanosystems Engineering Research Center for Nanotechnology-Enabled Water Treatment, Houston, Texas 77005, United States*

Manav Bhati − *Department of Chemical and Biomolecular Engineering, Rice University, Houston, Texas 77005-1892, United States; Nanosystems Engineering Research Center for Nanotechnology-Enabled Water Treatment, Houston, Texas 77005, United States*

Benjamin W. Walls − *Department of Chemical and Biomolecular Engineering, Rice University, Houston, Texas 77005-1892, United States*

Bo Wang − *Department of Chemical and Biomolecular Engineering, Rice University, Houston, Texas 77005-1892, United States; Nanosystems Engineering Research Center for Nanotechnology-Enabled Water Treatment, Houston, Texas 77005, United States*

Michael S. Wong − *Department of Chemical and Biomolecular Engineering, Rice University, Houston, Texas 77005-1892, United States; Nanosystems Engineering Research Center for Nanotechnology-Enabled Water Treatment, Houston, Texas 77005, United States; Department of Environmental Engineering, Department of Chemistry, and Department of Materials Science and NanoEngineering, Rice University, Houston, Texas 77005, United States;* ⓞ orcid.org/0000-0002-3652-3378

Complete contact information is available at:
https://pubs.acs.org/10.1021/acs.est.2c01637

Author Contributions
#Y.C. and M.B. contributed equally to this work.

Notes
The authors declare no competing financial interest.

■ REFERENCES
(1) Liu, X.; Wei, W.; Xu, J.; Wang, D.; Song, L.; Ni, B.-J. Photochemical Decomposition of Perfluorochemicals in Contaminated Water. *Water Res.* **2020**, *186*, No. 116311.
(2) Kwiatkowski, C. F.; Andrews, D. Q.; Birnbaum, L. S.; Bruton, T. A.; DeWitt, J. C.; Knappe, D. R. U.; Maffini, M. V.; Miller, M. F.; Pelch, K. E.; Reade, A.; Soehl, A.; Trier, X.; Venier, M.; Wagner, C.

C.; Wang, Z.; Blum, A. Scientific Basis for Managing PFAS as a Chemical Class. *Environ. Sci. Technol. Lett.* **2020**, 7, 532–543.

(3) Buck, R. C.; Franklin, J.; Berger, U.; Conder, J. M.; Cousins, I. T.; de Voogt, P.; Jensen, A. A.; Kannan, K.; Mabury, S. A.; van Leeuwen, S. P. Perfluoroalkyl and Polyfluoroalkyl Substances in the Environment: Terminology, Classification, and Origins. *Integr. Environ. Assess. Manag.* **2011**, 7, 513–541.

(4) Duan, L.; Wang, B.; Heck, K.; Guo, S.; Clark, C. A.; Arredondo, J.; Wang, M.; Senftle, T. P.; Westerhoff, P.; Wen, X.; Song, Y.; Wong, M. S. Efficient Photocatalytic PFOA Degradation over Boron Nitride. *Environ. Sci. Technol. Lett.* **2020**, 7, 613–619.

(5) Wickramaratne, D.; Weston, L.; Van de Walle, C. G. Monolayer to Bulk Properties of Hexagonal Boron Nitride. *J. Phys. Chem. C* **2018**, 122, 25524–25529.

(6) Wan, Q.; Wei, F.; Ma, Z.; Anpo, M.; Lin, S. Novel Porous Boron Nitride Nanosheet with Carbon Doping: Potential Metal-Free Photocatalyst for Visible-Light-Driven Overall Water Splitting. *Adv. Theory Simul.* **2019**, 2, No. 1800174.

(7) Li, X.; Li, Z.; Yang, J. Proposed Photosynthesis Method for Producing Hydrogen from Dissociated Water Molecules Using Incident Near-Infrared Light. *Phys. Rev. Lett.* **2014**, 112, No. 018301.

(8) Singh, B.; Kaur, G.; Singh, P.; Singh, K.; Sharma, J.; Kumar, M.; Bala, R.; Meena, R.; Sharma, S. K.; Kumar, A. Nanostructured BN–TiO2 Composite with Ultra-High Photocatalytic Activity. *New J. Chem.* **2017**, 41, 11640–11646.

(9) Fu, X.; Hu, Y.; Yang, Y.; Liu, W.; Chen, S. Ball Milled H-BN: An Efficient Holes Transfer Promoter to Enhance the Photocatalytic Performance of TiO2. *J. Hazard. Mater.* **2013**, 244-245, 102–110.

(10) Dorn, R. W.; Ryan, M. J.; Kim, T.-H.; Goh, T. W.; Venkatesh, A.; Heintz, P. M.; Zhou, L.; Huang, W.; Rossini, A. J. Identifying the Molecular Edge Termination of Exfoliated Hexagonal Boron Nitride Nanosheets with Solid-State NMR Spectroscopy and Plane-Wave DFT Calculations. *Chem. Mater.* **2020**, 32, 3109–3121.

(11) Weston, L.; Wickramaratne, D.; Mackoit, M.; Alkauskas, A.; Van de Walle, C. G. Native Point Defects and Impurities in Hexagonal Boron Nitride. *Phys. Rev. B* **2018**, 97, No. 214104.

(12) Salavati-fard, t.; Wang, B. Significant Role of Oxygen Dopants in Photocatalytic PFCA Degradation over H-BN. *ACS Appl. Mater. Interfaces* **2021**, 13, 46727–46737.

(13) Fang, C.; Megharaj, M.; Naidu, R. Electrochemical Advanced Oxidation Processes (EAOP) to Degrade per- and Polyfluoroalkyl Substances (PFASs). *J. Adv. Oxid. Technol.* **2017**, 20 (), DOI: 10.1515/jaots-2017-0014.

(14) Niu, J.; Lin, H.; Xu, J.; Wu, H.; Li, Y. Electrochemical Mineralization of Perfluorocarboxylic Acids (PFCAs) by Ce-Doped Modified Porous Nanocrystalline PbO2 Film Electrode. *Environ. Sci. Technol.* **2012**, 46, 10191–10198.

(15) Liu, Y.; Chen, S.; Quan, X.; Yu, H.; Zhao, H.; Zhang, Y. Efficient Mineralization of Perfluorooctanoate by Electro-Fenton with H2O2 Electro-Generated on Hierarchically Porous Carbon. *Environ. Sci. Technol.* **2015**, 49, 13528–13533.

(16) Plumlee, M. H.; McNeill, K.; Reinhard, M. Indirect Photolysis of Perfluorochemicals: Hydroxyl Radical-Initiated Oxidation of N-Ethyl Perfluorooctane Sulfonamido Acetate (N-EtFOSAA) and Other Perfluoroalkanesulfonamides. *Environ. Sci. Technol.* **2009**, 43, 3662–3668.

(17) D'eon, J.; Hurley, M. D.; Wallington, T. J.; Mabury, S. A. Atmospheric Chemistry of N-Methyl Perfluorobutane Sulfonamidoethanol, C4F9SO2N (CH3)CH2CH2OH: Kinetics and Mechanism of Reaction with OH. *Environ. Sci. Technol.* **2006**, 40, 1862–1868.

(18) Kutsuna, S.; Hori, H. Rate Constants for Aqueous-Phase Reactions of SO4− with C2F5C(O)O− and C3F7C(O)O− at 298 K. *Int. J. Chem. Kinet.* **2007**, 39, 276–288.

(19) Hori, H.; Nagaoka, Y.; Murayama, M.; Kutsuna, S. Efficient Decomposition of Perfluorocarboxylic Acids and Alternative Fluorochemical Surfactants in Hot Water. *Environ. Sci. Technol.* **2008**, 42, 7438–7443.

(20) Nohara, K.; Toma, M.; Kutsuna, S.; Takeuchi, K.; Ibusuki, T. Cl Atom-Initiated Oxidation of Three Homologous Methyl Perfluoroalkyl Ethers. *Environ. Sci. Technol.* **2001**, 35, 114–120.

(21) Wallington, T. J.; Hurley, M. D.; Fracheboud, J. M.; Orlando, J. J.; Tyndall, G. S.; Sehested, J.; Møgelberg, T. E.; Nielsen, O. J. Role of Excited CF3CFHO Radicals in the Atmospheric Chemistry of HFC-134a. *J. Phys. Chem.* **1996**, 100, 18116–18122.

(22) Zhang, Y.; Moores, A.; Liu, J.; Ghoshal, S. New Insights into the Degradation Mechanism of Perfluorooctanoic Acid by Persulfate from Density Functional Theory and Experimental Data. *Environ. Sci. Technol.* **2019**, 53, 8672–8681.

(23) Ellis, D. A.; Martin, J. W.; De Silva, A. O.; Mabury, S. A.; Hurley, M. D.; Sulbaek Andersen, M. P.; Wallington, T. J. Degradation of Fluorotelomer Alcohols: A Likely Atmospheric Source of Perfluorinated Carboxylic Acids. *Environ. Sci. Technol.* **2004**, 38, 3316–3321.

(24) Zhuo, Q.; Deng, S.; Yang, B.; Huang, J.; Yu, G. Efficient Electrochemical Oxidation of Perfluorooctanoate Using a Ti/SnO2-Sb-Bi Anode. *Environ. Sci. Technol.* **2011**, 45, 2973–2979.

(25) Kresse, G.; Furthmüller, J. Efficient Iterative Schemes for Ab Initio Total-Energy Calculations Using a Plane-Wave Basis Set. *Phys. Rev. B* **1996**, 54, 11169–11186.

(26) Kresse, G.; Furthmüller, J. Efficiency of Ab-Initio Total Energy Calculations for Metals and Semiconductors Using a Plane-Wave Basis Set. *Comput. Mater. Sci.* **1996**, 6, 15–50.

(27) Silverstein, T. P. Marcus Theory: Thermodynamics CAN Control the Kinetics of Electron Transfer Reactions. *J. Chem. Educ.* **2012**, 89, 1159–1167.

(28) Chaudhuri, S.; Hedström, S.; Méndez-Hernández, D. D.; Hendrickson, H. P.; Jung, K. A.; Ho, J.; Batista, V. S. Electron Transfer Assisted by Vibronic Coupling from Multiple Modes. *J. Chem. Theory Comput.* **2017**, 13, 6000–6009.

(29) Hörmann, N. G.; Andreussi, O.; Marzari, N. Grand Canonical Simulations of Electrochemical Interfaces in Implicit Solvation Models. *J. Chem. Phys.* **2019**, 150, No. 041730.

(30) Melander, M. M.; Kuisma, M. J.; Christensen, T. E. K.; Honkala, K. Grand-Canonical Approach to Density Functional Theory of Electrocatalytic Systems: Thermodynamics of Solid-Liquid Interfaces at Constant Ion and Electrode Potentials. *J. Chem. Phys.* **2019**, 150, No. 041706.

(31) Van den Bossche, M.; Skúlason, E.; Rose-Petruck, C.; Jónsson, H. Assessment of Constant-Potential Implicit Solvation Calculations of Electrochemical Energy Barriers for H2 Evolution on Pt. *J. Phys. Chem. C* **2019**, 123, 4116–4124.

(32) Lindgren, P.; Kastlunger, G.; Peterson, A. A. A Challenge to the G ∼ 0 Interpretation of Hydrogen Evolution. *ACS Catal.* **2020**, 10, 121–128.

(33) Bhati, M.; Chen, Y.; Senftle, T. P. Density Functional Theory Modeling of Photo-Electrochemical Reactions on Semiconductors: H2 Evolution on 3C-SiC. *J. Phys. Chem. C* **2020**, 124, 26625.

(34) Mathew, K.; Kolluru, V. S. C.; Mula, S.; Steinmann, S. N.; Hennig, R. G. Implicit Self-Consistent Electrolyte Model in Plane-Wave Density-Functional Theory. *J. Chem. Phys.* **2019**, 151, 234101.

(35) Mathew, K.; Sundararaman, R.; Letchworth-Weaver, K.; Arias, T. A.; Hennig, R. G. Implicit Solvation Model for Density-Functional Study of Nanocrystal Surfaces and Reaction Pathways. *J. Chem. Phys.* **2014**, 140, No. 084106.

(36) Trasatti, S. The absolute electrode potential: an explanatory note (Recommendations 1986). *Pure Appl. Chem.* **1986**, 58, 955–966.

(37) Collin, F. Chemical Basis of Reactive Oxygen Species Reactivity and Involvement in Neurodegenerative Diseases. *Int. J. Mol. Sci.* **2019**, 20, 2407.

(38) Wardman, P. Reduction Potentials of One-Electron Couples Involving Free Radicals in Aqueous Solution. *J. Phys. Chem. Ref. Data* **1989**, 18, 1637–1755.

(39) Weber, M.; Koonkaew, B.; Balme, S.; Utke, I.; Picaud, F.; Iatsunskyi, I.; Coy, E.; Miele, P.; Bechelany, M. Boron Nitride Nanoporous Membranes with High Surface Charge by Atomic Layer Deposition. *ACS Appl. Mater. Interfaces* **2017**, 9, 16669–16678.

(40) Siria, A.; Poncharal, P.; Biance, A.-L.; Fulcrand, R.; Blase, X.; Purcell, S. T.; Bocquet, L. Giant Osmotic Energy Conversion Measured in a Single Transmembrane Boron Nitride Nanotube. *Nature* **2013**, *494*, 455−458.

(41) Shi, C.; O'Grady, C. P.; Peterson, A. A.; Hansen, H. A.; Nørskov, J. K. Modeling CO2 Reduction on Pt(111). *Phys. Chem. Chem. Phys.* **2013**, *15*, 7114−7122.

(42) Nosaka, Y.; Nosaka, A. Understanding Hydroxyl Radical (·OH) Generation Processes in Photocatalysis. *ACS Energy Lett.* **2016**, *1*, 356−359.

(43) Alem, N.; Erni, R.; Kisielowski, C.; Rossell, M. D.; Gannett, W.; Zettl, A. Atomically Thin Hexagonal Boron Nitride Probed by Ultrahigh-Resolution Transmission Electron Microscopy. *Phys. Rev. B* **2009**, *80*, No. 155425.

(44) Liu, D.; Zhang, M.; Xie, W.; Sun, L.; Chen, Y.; Lei, W. Porous BN/TiO2 Hybrid Nanosheets as Highly Efficient Visible-Light-Driven Photocatalysts. *Appl. Catal. B Environ.* **2017**, *207*, 72−78.

(45) He, Z.; Kim, C.; Jeon, T. H.; Choi, W. Hydrogenated Heterojunction of Boron Nitride and Titania Enables the Photo-catalytic Generation of H2 in the Absence of Noble Metal Catalysts. *Appl. Catal. B Environ.* **2018**, *237*, 772−782.

(46) Gouin, X.; Grange, P.; Bois, L.; L'Haridon, P.; Laurent, Y. Characterization of the Nitridation Process of Boric Acid. *J. Alloys Compd.* **1995**, *224*, 22−28.

(47) Strohmeier, B. R. Surface Characterization of Aluminum Foil Annealed in the Presence of Ammonium Fluoborate. *Appl. Surf. Sci.* **1989**, *40*, 249−263.

(48) Smith McWilliams, A. D.; Martínez-Jiménez, C.; Matatyaho Ya'akobi, A.; Ginestra, C. J.; Talmon, Y.; Pasquali, M.; Martí, A. A. Understanding the Exfoliation and Dispersion of Hexagonal Boron Nitride Nanosheets by Surfactants: Implications for Antibacterial and Thermally Resistant Coatings. *ACS Appl. Nano Mater.* **2021**, *4*, 142−151.

(49) Bratsch, S. G. Standard Electrode Potentials and Temperature Coefficients in Water at 298.15 K. *J. Phys. Chem. Ref. Data* **1989**, *18*, 1−21.

(50) Perdew, J. P.; Burke, K.; Ernzerhof, M. Generalized Gradient Approximation Made Simple. *Phys. Rev. Lett.* **1996**, *77*, 3865−3868.

(51) Sun, J.; Ruzsinszky, A.; Perdew, J. P. Strongly Constrained and Appropriately Normed Semilocal Density Functional. *Phys. Rev. Lett.* **2015**, *115*, No. 036402.

(52) Ambrosio, F.; Wiktor, J.; Angelis, F. D.; Pasquarello, A. Origin of Low Electron−Hole Recombination Rate in Metal Halide Perovskites. *Energy Environ. Sci.* **2018**, *11*, 101−105.

(53) Zhang, J.; Sun, R.; Ruan, D.; Zhang, M.; Li, Y.; Zhang, K.; Cheng, F.; Wang, Z.; Wang, Z.-M. Point Defects in Two-Dimensional Hexagonal Boron Nitride: A Perspective. *J. Appl. Phys.* **2020**, *128*, 100902.

(54) Li, Z.; Wei, W.; Li, H.; Li, S.; Leng, L.; Zhang, M.; Horton, J. H.; Wang, D.; Sun, W.; Guo, C.; Wu, W.; Wang, J. Low-Temperature Synthesis of Single Palladium Atoms Supported on Defective Hexagonal Boron Nitride Nanosheet for Chemoselective Hydrogenation of Cinnamaldehyde. *ACS Nano* **2021**, *15*, 10175−10184.

(55) Ding, Y.; Torres-Davila, F.; Khater, A.; Nash, D.; Blair, R.; Tetard, L. Defect Engineering in Boron Nitride for Catalysis. *MRS Commun.* **2018**, *8*, 1236−1243.

(56) Takacs, L. Self-Sustaining Reactions Induced by Ball Milling. *Prog. Mater. Sci.* **2002**, *47*, 355−414.